EPSL

Sizing up crystals and their melt inclusions: a new approach to crystallization studies

Kurt Roggensack *

Department of Geology, Arizona State University, Tempe, AZ 85287-1404, USA

Abstract

A correlation between melt inclusion composition and host crystal size has been discovered in a basaltic ash deposit from a volcanic arc setting. Least-evolved melt inclusions, featuring high H_2O–CO_2 saturation pressures, are found in large olivine crystals. Melt inclusion compositions become more evolved and volatile saturation pressures decrease as host crystal size decreases. This trend is interpreted as reflecting crystal nucleation and growth during decompression of a magma saturated with H_2O and CO_2. In general, melt inclusion compositions show large incompatible element enrichment and modest major element variation consistent with in situ crystallization. Crystal size is used to temporally constrain the formation age of melt inclusions and the decompression path of the magma. An estimated crystal growth rate of 10^{-8} cm s^{-1} yields an initial average magma ascent rate of ~ 4.8 km yr^{-1} at mid-crustal depths. At shallower depths the ascent rate was roughly an order of magnitude greater. © 2001 Elsevier Science B.V. All rights reserved.

Keywords: volatiles; degassing; melts; inclusions; in situ crystallization

1. Introduction

The process of magma crystallization does not easily lend itself to direct observation. Typically, crystallization studies rely on theoretical approaches [1], analog systems [2], experiments [3] or the study of the end products after crystallization has stopped or been artificially arrested [4–6]. This study attempts to link melt inclusion and textural (e.g. crystal size) data to constrain magma crystallization. This new approach has the po-

tential to provide new information on crystallization processes of natural magmas.

It might be expected that crystal size and melt inclusion compositions should show some type of correlation. In an evolving magma both crystal growth and magma composition are time-dependent. What is uncertain is the timing of individual melt inclusion formation. The possibility that melt inclusions might form at different stages of crystal growth obscures the relationship between crystal age and melt inclusion age. Despite this uncertainty, it will be shown that useful information may still be obtained by relating crystal size to melt inclusion composition.

Consider a simple model of crystallization occurring in a closed system (Fig. 1). In such a system, incompatible element enrichment is always

* Tel.: +1-480-965-9852; Fax: +1-480-965-8102;
E-mail: kurt.roggensack@asu.edu

progressive and the rate of enrichment increases as the amount of magma decreases. It is also true that crystals growing in a simple system will show a relationship between size and age. The larger the crystal the greater the crystal's age. Now consider how crystal age might be related to melt inclusion composition. Because the magma composition is progressively evolving, only crystals which nucleate early in the crystallization sequence are capable of sampling unevolved, incompatible element-poor magma. In contrast, crystals which nucleate late in the crystallization sequence may only trap evolved, incompatible element-rich magma. This demonstrates a relationship between the host crystal age and the melt inclusion composition. As crystal age decreases (i.e. crystal size decreases) the *minimum level* of incompatible element enrichment *increases* in melt inclusions.

Given this simple model of crystallization it is useful to consider the magma's changing rate of incompatible element enrichment and the relative timing of melt inclusion formation. Since incompatible element enrichment is initially slow, it is expected that melt inclusions trapped during the early stages of crystallization should show little compositional variability (inset A, Fig. 2). Later, when incompatible element enrichment is more rapid, melt inclusions should show more composi-

Fig. 2. Crystal mass and melt inclusion relationships for fractional crystallization of a closed system. The curve represents magma composition where crystal mass is a (non-linear) proxy for time. Note that the *minimum* concentration of K_2O in melt inclusions increases as crystal mass decreases. If crystals form multiple melt inclusions over time, younger melt inclusions will plot toward increasing K_2O (tie-lines). Also, note how the magma's changing rate of incompatible element enrichment influences melt inclusion compositions. During the early stages of crystallization, the enrichment is relatively slow. Melt inclusions formed during this period will be similar in composition regardless of their relative age (on or above curve, inset A). Later, when enrichment is more rapid, melt inclusions of closely similar age may be compositionally dissimilar (on or above curve, inset B). Bulk composition is similar to low-K_2O melt inclusions, whereas matrix glass is similar to high-K_2O melt inclusions.
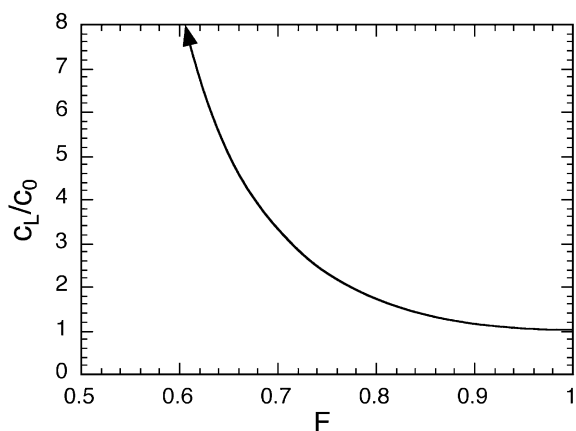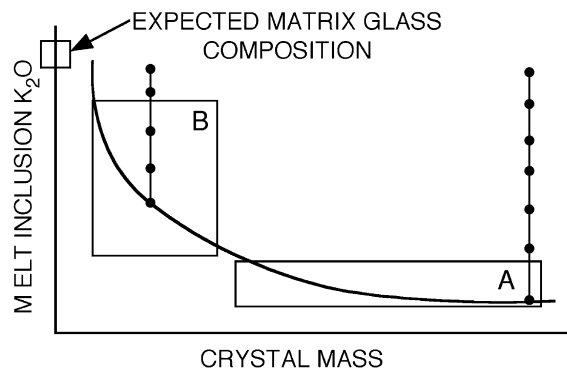

Fig. 1. Enrichment of a perfectly incompatible element during fractional crystallization (i.e. Rayleigh fractionation). F is the fraction of liquid remaining, C_L is the concentration of the trace element in the liquid, C_O is the original concentration of the trace element. Note how the rate of enrichment increases with time.

tional variability (inset B, Fig. 2). At the later stages of crystallization even melt inclusions of roughly similar age could show significant compositional differences. The timing of melt inclusion formation may also be important. For simplicity consider several crystals of contrasting age (i.e. size) that trap several melt inclusions. Within a given crystal, early-formed melt inclusions will always be less incompatible element-enriched than later-formed melt inclusions. It follows that all melt inclusion compositions, regardless of host crystal size, should plot either on or above a curve defined by the magma's progressive incompatible element enrichment (Fig. 2). Early-forming melt inclusions (i.e. melt inclusions that form shortly after crystal nucleation) should plot on the curve whereas late-forming melt inclusions will plot above the curve.

One last feature of this simple model regards the fact that in a closed system the bulk compo-
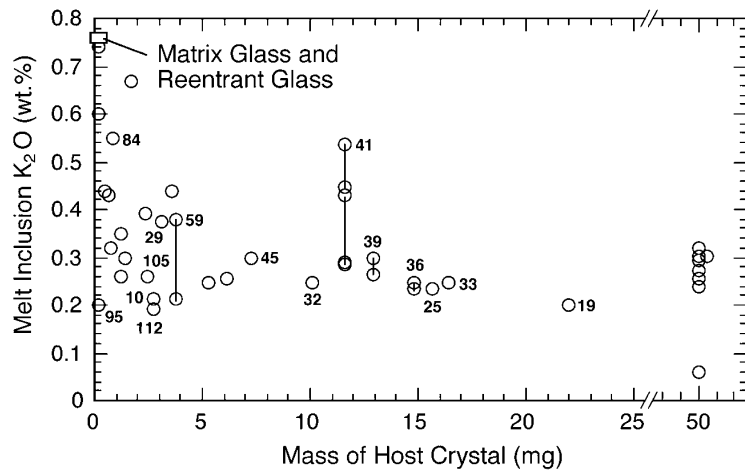
Fig. 3. Host crystal mass versus melt inclusion composition. Select crystals are identified by sample number. Tie-lines join crystals that host multiple melt inclusions.

sition does not change. The earliest-formed (i.e. oldest) melt inclusions should be compositionally similar to the bulk magma. In contrast, the latest-formed melt inclusions should be compositionally similar to the matrix glass.

A recent basaltic ash deposit from the Cerro Negro volcano, in Nicaragua, displays a correlation between crystal size and melt inclusion composition (Fig. 3) similar to the hypothetical model. Large crystals contain relatively primitive (low-K_2O) melt inclusions, whereas small crystals contain more evolved melt inclusions. It will be shown that these data provide spatial (volatile saturation pressures), temporal (crystal size), and compositional (melt inclusion composition) information that constrains the dynamic evolution of a natural magma. The results have implications for understanding arc magma petrogenesis (e.g. water abundance in primitive magmas) as well as volcanic processes.

2. Analytical methods

Data presented herein are from a bulk ash sample ($\sim$30 g) from the Cerro Negro volcano in Nicaragua [7,8]. The sample was collected from a pit dug in the ash blanket roughly 2 km SSW of the vent. This sample is assigned to Cerro Ne-

gro's 1867 eruption based on historical records and stratigraphic relationships [9]. Initially, 71 olivine crystals were randomly handpicked and individually weighed. The minor mass contribution of attached microlites and matrix glass was ignored. Although preference was given to unbroken crystals, in some cases it was possible to estimate the original crystal mass of broken crystals based on visual study of the crystal form. Later, 37 additional crystals were selected and weighed to extend the data to include the smallest crystal size fraction. During selection this second group of crystals (all but two < 0.00270 g) were visually compared to each other in an attempt to ensure that all crystal sizes were represented. For this reason, this group of small crystals does not represent a random sample and these data are not included in the crystal size distribution (CSD) analysis.

In preparation for melt inclusion study, all olivine crystals were individually mounted in epoxy then optically searched to identify primary, unfractured melt inclusions. In some cases it was necessary to lightly polish the epoxy mounts to remove matrix glass and improve the light transmittance through the crystals. From the subgroup of crystals containing suitable melt inclusions, samples were selected for analysis based on crystal mass, the goal being to obtain crystals spanning

Table 1
Major element analyses of melt inclusions and bulk ash

Sample	SiO$_2$	TiO$_2$	Al$_2$O$_3$	FeO*	MnO	MgO	CaO	Na$_2$O	K$_2$O	P$_2$O$_5$	SO$_3$	Cl	Orig.	Mass (mg)	Olivine Fo MI	Rim
Melt inclusion analyses																
10	47.96	0.78	18.77	10.92	0.15	6.86	12.23	1.95	0.21	0.17	0.32	0.08	94.43	2.74	80	n.d.
19	49.64	0.71	18.05	10.54	0.19	6.43	12.09	1.99	0.20	0.17	0.22	0.06	95.15	21.99	81	81
25	50.32	0.72	18.03	10.11	0.14	5.65	12.78	1.80	0.24	0.23	0.30	0.06	93.65	15.67	n.d.	n.d.
29	50.86	0.77	18.33	9.58	0.00	5.66	12.17	2.10	0.37	0.15	0.37	0.08	94.25	3.07	81	79
31	48.65	0.73	18.51	10.84	0.23	5.98	12.96	1.79	0.25	0.08	0.37	0.08	93.97	5.31	81	79
32[a]	49.63	0.72	18.49	10.33	0.15	6.65	11.85	1.93	0.25	0.00	0.00	0.06	92.98	10.08	80	79
33	49.61	0.80	19.07	9.68	0.00	5.05	13.17	2.27	0.25	0.10	0.32	0.09	93.64	16.46	82	83
35	50.61	0.85	18.31	9.02	0.15	5.53	12.89	2.23	0.30	0.12	0.30	0.06	94.25	50.85	n.d.	n.d.
36a	49.77	0.81	18.55	10.07	0.00	5.42	13.19	1.95	0.25	0.00	0.32	0.08	93.07	14.85	82	77
36b	49.67	0.61	18.22	9.79	0.18	6.84	12.52	1.91	0.25	0.00	0.22	0.04	93.38	14.85	82	77
36c	49.04	0.82	18.62	10.29	0.18	5.83	12.81	2.10	0.23	0.08	0.37	0.08	94.33	14.85	n.d.	77
39a[b]	47.86	1.30	18.30	10.62	0.19	6.82	12.10	2.29	0.30	0.22	0.27	0.06	93.90	12.96	82	81
39b	50.23	0.80	17.78	9.78	0.16	7.14	11.73	2.02	0.27	0.10	0.30	0.05	94.48	12.96	82	81
41a[b]	48.18	0.90	17.92	12.43	0.19	5.75	11.89	2.29	0.29	0.17	0.20	0.09	95.19	11.60	76	76
41b	50.42	0.94	17.23	11.58	0.34	5.68	10.13	3.00	0.54	0.15	0.00	0.11	95.41	11.60	77	76
41c	50.51	0.96	17.37	11.35	0.16	5.71	10.81	2.56	0.43	0.15	0.17	0.12	95.94	11.60	n.d.	76
41d	49.12	0.96	17.42	12.50	0.31	5.71	11.11	2.25	0.45	0.19	0.15	0.08	96.45	11.60	n.d.	76
41e	48.85	0.79	18.28	11.86	0.22	5.87	11.30	2.36	0.29	0.19	0.22	0.10	97.34	11.60	n.d.	76
45	49.09	0.72	18.67	10.25	0.18	6.36	12.36	2.01	0.30	0.05	0.35	0.06	94.73	7.28	82	80
51	48.97	0.80	18.37	9.89	0.13	5.96	13.64	1.89	0.26	0.10	0.37	0.06	93.96	6.12	83	82
59a	49.63	1.00	18.05	10.06	0.16	6.79	11.33	2.20	0.38	0.41	0.30	0.05	95.09	3.80	81	81
59b	48.71	0.72	18.42	10.55	0.29	7.08	12.10	1.93	0.21	0.00	0.35	0.08	94.68	3.80	81	81
65	48.79	0.77	18.08	10.01	0.29	7.05	12.84	1.85	0.27	0.05	0.30	0.07	94.03	~50.00	n.d.	n.d.
66	49.77	0.77	18.39	10.96	0.22	5.40	11.91	2.26	0.23	0.10	0.22	0.10	94.23	~50.00	n.d.	n.d.
70	49.88	0.73	18.18	10.11	0.22	5.98	12.50	2.02	0.29	0.10	0.30	0.08	94.01	~50.00	n.d.	n.d.
71	48.91	0.88	19.24	10.12	0.14	5.19	12.77	2.22	0.32	0.22	0.27	0.06	94.93	~50.00	n.d.	n.d.
72	49.47	0.74	18.33	9.99	0.13	7.36	11.60	2.03	0.25	0.12	0.32	0.06	95.65	~50.00	82	81
73	48.60	0.32	18.32	10.48	0.18	6.96	13.70	1.38	0.05	0.00	0.07	0.02	93.20	~50.00	n.d.	n.d.
74	49.73	0.85	18.75	10.50	0.19	5.37	11.96	2.30	0.30	0.05	0.32	0.06	94.77	~50.00	80	81
75	49.03	0.77	18.40	9.91	0.18	6.69	12.77	1.90	0.27	0.08	0.27	0.07	93.37	~50.00	n.d.	n.d.
80	49.86	0.80	18.30	10.73	0.22	5.15	12.25	2.25	0.30	0.15	0.35	0.06	94.46	1.39	n.d.	n.d.
82	51.37	1.17	16.56	12.65	0.32	4.70	9.70	2.71	0.60	0.22	0.00	0.13	95.64	0.16	73	73
84	51.11	1.08	16.32	12.05	0.24	5.61	10.02	2.78	0.55	0.24	0.30	0.09	96.16	0.88	74	72
87	51.08	0.97	16.01	13.50	0.29	5.11	9.92	2.53	0.44	0.17	0.07	0.10	96.26	0.48	n.d.	n.d.
91	49.96	0.83	17.63	10.44	0.18	6.77	11.62	2.17	0.39	0.00	0.42	0.04	93.07	2.40	n.d.	n.d.
93	51.56	1.05	16.66	12.38	0.19	4.45	10.19	2.95	0.43	0.15	0.20	0.09	95.31	0.69	n.d.	n.d.
95	48.18	0.76	17.69	12.23	0.24	6.76	11.89	1.97	0.20	0.07	0.35	0.07	94.73	0.23	78	75
96	51.18	1.50	16.22	12.84	0.23	4.24	9.90	2.99	0.74	0.17	0.15	0.13	95.86	0.17	n.d.	n.d.
103	50.49	0.77	17.51	10.67	0.19	5.93	11.33	2.46	0.32	0.34	0.02	0.07	94.93	0.77	n.d.	n.d.
104	53.24	1.08	15.71	12.10	0.25	4.32	9.68	2.80	0.67	0.16	0.15	0.13	90.50	1.68	n.d.	n.d.
105	50.49	0.73	17.40	10.57	0.18	6.84	11.02	2.34	0.26	0.17	0.25	0.07	93.49	2.41	n.d.	n.d.
107	50.73	0.89	18.30	10.03	0.18	4.51	12.11	2.73	0.44	0.10	0.32	0.12	94.20	3.61	n.d.	n.d.
109	49.28	0.86	18.61	10.66	0.25	5.07	12.90	1.98	0.26	0.15	0.27	0.08	93.86	1.25	n.d.	n.d.
112	49.22	0.78	18.76	10.33	0.19	5.53	12.70	2.20	0.19	0.10	0.32	0.09	93.95	2.73	80	74
113	51.22	0.93	17.22	10.01	0.16	6.33	11.45	2.20	0.35	0.15	0.15	0.07	94.84	1.19	n.d.	n.d.
Matrix glass and re-entrant analyses																
87MG	53.94	1.68	13.29	14.73	0.19	3.41	8.97	2.83	0.77	0.19	0.00	0.10	99.73	NA	NA	NA
104RE	52.90	1.22	14.38	13.36	0.28	3.86	9.81	3.21	0.74	0.22	0.00	0.14	99.74	NA	NA	NA
Bulk ash analyses																
CN	49.11	0.68	17.09	9.59	0.19	8.13	13.08	1.73	0.30	0.09	n.d.	n.d.	99.28	NA	NA	NA
CN[c]	49.41	0.71	18.80	9.07	0.19	6.88	12.66	1.85	0.33	0.10	n.d.	n.d.	99.27	NA	NA	NA

Table 1 (*continued*)

FeO*, total iron as FeO. Orig. represents original analysis total before normalization to 100% on a volatile-free basis. Mass refers to host crystal. Approximate masses (crystals 65–75) based on dimensions of crystal fragments. Olivine compositions measured near ($\sim$10 μm) melt inclusion (MI) or crystal rim (Rim). n.d., not determined. NA, not applicable. Scoria mode based on counting 1000 points: 36% crystals; plagioclase 22%, olivine 8%, clinopyroxene 5%, trace magnetite.
[a]Superscript identifies melt inclusions which contain daughter crystals of plagioclase.
[b]Superscript identifies melt inclusions which contain daughter crystals of magnetite.
[c]Large phenocrysts removed by handpicking.

the entire observed mass range. These crystals were polished by hand to expose the melt inclusions for analysis. The major elements, S and Cl were analyzed by electron microprobe at Arizona State University using a JEOL-8600 Superprobe and natural and synthetic standards. An accelerating voltage of 15 kV and sample current of 10 nA were used during analysis. Data were corrected using a ZAF routine. Mineral analyses were made with a focused beam (1–2 μm diameter), whereas glasses were analyzed with a 10–15 μm diameter beam. Counting times for Na in glass were limited to 10 s to minimize Na loss. Melt inclusion analyses in most cases represent a single analysis point. Backscatter electron imaging was used to check for incipient devitrification (rare). X-ray fluorescence (XRF) major and trace element data on bulk ash are from Washington State University.

Melt inclusion water contents were determined by Fourier transform infrared spectroscopy (FTIR) at the laboratory of Dr. J. Lowenstern at USGS in Menlo Park, CA. Analyses were made using a Nicolet Magna IR spectrometer 750 with a Spectra Tech IR Plan analytical microscope [10]. Crystal wafers containing melt inclusions were centered over large apertures and the portion of the melt inclusion to be analyzed (typically 20–40 μm square area) was selected by closing the microscope apertures. Vapor bubbles, present in nearly all melt inclusions, were avoided during analysis. Typical analyses employed 1024 scans. Melt inclusion thicknesses were measured by viewing the crystal wafer edgewise under high magnification [11]. Estimates based on replicate analyses and comparison with backscatter electron images indicates thickness errors are less than several micrometers. Water concentrations were determined from absorbance peak heights on the 1630 cm^{-1}, 3570 cm^{-1}, 4500 cm^{-1}, and 5200 cm^{-1} bands using basalt extinction coefficients (28, 63, 0.67, and 0.62, respectively [12,13]). Note that the extinction coefficient for the 1630 cm^{-1} band is sensitive to melt composition and the value of 28 used here, which represents the high end of the range [13], gave best agreement with the 5200 cm^{-1} band. CO_2 (as carbonate) concentrations were from absorbance peak heights on the $\sim$1430 cm^{-1} and $\sim$1510 cm^{-1} bands using a basalt extinction coefficient (375 [14]). For all spectra, the backgrounds for measuring peak heights were drawn by hand using a set of French curves. Glass densities were assumed to be constant at 2800 g cm^{-3}.

Trace element analyses of melt inclusions were made with a Cameca 3f ion probe in the Arizona State University Center for Solid State Science. Sample surfaces were first cleaned by polishing with diamond powder suspended in distilled water and then prepared for analysis by coating with Au. A $^{16}O^{-}$ primary ion beam ($\sim$1 nA) was focused to a $\sim$15 μm spot and directed at areas of interest on the sample. The analysis area was initially sputtered for 7 minutes to remove any possible surface contaminants and allow the secondary beam to stabilize before collecting data. Positive secondary ions with 75 ± 20 eV excess kinetic energy were allowed into the mass spectrometer. This degree of 'energy filtering' of the secondary ion beam effectively eliminates complex molecular ions from the mass spectrum, thus allowing most elements to be detected without interferences at the same nominal mass:charge ratio [15]. Analytical error on trace element analyses are $<10\%$ based on counting statistics.

3. Cerro Negro background

Cerro Negro is a part of the El Hoyo–Las Pilas

volcanic complex located in western Nicaragua. The morphology of Cerro Negro resembles that of a monogenetic cinder cone although the frequent activity of the volcano more closely resembles that of a polygenetic stratovolcano. Since Cerro Negro's initial eruption in 1850, there have been more than 20 eruptions. The more recent series of eruptions in the last 80 years show an apparent periodicity [9,16]. On the basis of stratigraphic relationships the ash deposit discussed here has been assigned to the second Cerro Negro eruption which occurred in 1867 [9]. In general, the volumes of all but the most recent Cerro Negro eruptions are poorly known. Volume estimates of the first two eruptions are ∼0.006 and 0.010 km³, respectively [9,16]. Like the more recent eruptions of Cerro Negro [7], the 1867 deposit is a high-alumina basalt containing abundant phenocrysts (∼36% by volume) of plagioclase, olivine, augite and magnetite (see Table 1).

4. Olivine mass and melt inclusion compositions

Olivine crystals from the 1867 ash are euhedral (Fig. 4) and fall into two distinct size groups. Most olivine crystals are <17 mg whereas a second, poorly defined group comprised mostly of crystal fragments have masses of ∼50 mg (Appendix A). Between these two extremes only four crystals were found with masses of ∼20–30 mg. Crystals occasionally display small resorbed areas
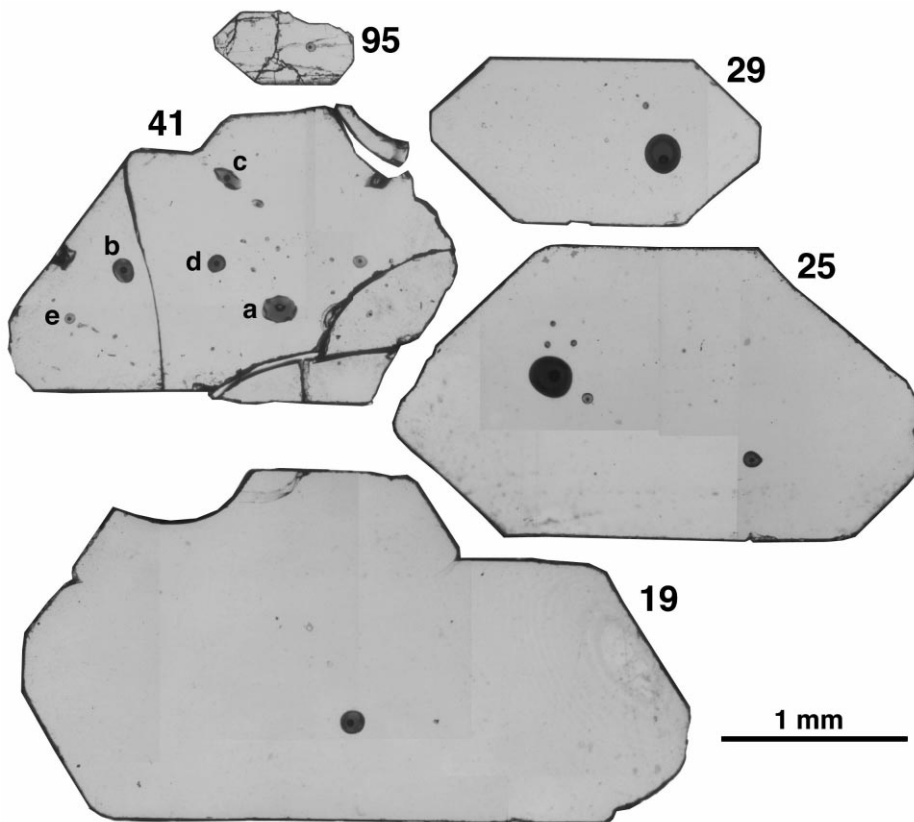

Fig. 4. Transmitted light photomicrograph of olivine crystals and melt inclusions sectioned for FTIR analysis. Original crystal mass ranges from 0.2 to 22 mg. Crystal #41 is unusual in that it hosts numerous melt inclusions spanning a large compositional range (e.g. 0.29–0.54 wt% K_2O).

(re-entrants) on their margins and joined crystals (synneusis [17]) appear to be relatively uncommon except for small (<2.7 mg) crystals. Almost all of the olivine crystals contain one or more melt inclusions, although in some cases the melt inclusions are too small to be analyzed or show signs of devitrification. The melt inclusions are typically round to ovoid in shape and contain a single vapor bubble. Melt inclusions which contain daughter crystals of anorthitic plagioclase ($\sim An_{94}$) or magnetite are compositionally similar to other melt inclusions (Table 1).

Most melt inclusions have high-alumina basalt compositions and show considerable compositional variation (Table 1). For example, K_2O ranges from 0.19 to 0.74 wt% with one exceptional melt inclusion (#73) having 0.05 wt% K_2O. Two melt inclusions (#39a and 96) have distinctively high TiO_2 although one of these has probably undergone Fe–Ti enrichment by low-pressure fractionation. Incompatible trace element compositions of the melt inclusions are also quite variable (Table 2). For instance, Zr and Y show large variation and correlate positively with K_2O. Melt inclusion #73 with exceptionally low K_2O is also characterized by low B, Zr, and Ba abundances. Despite the compositional variability of the melt inclusions, the host olivine compositions fall within a relatively restricted range Fo_{72-83} (Table 1). The lower forsterite compositions generally correlate with more evolved melt inclusions.

Crystals hosting several large (>50 μm) melt inclusions are relatively common. Whenever possible, these additional melt inclusions were analyzed to check the compositional variation preserved within a single crystal. Generally, the multiple melt inclusions in this eruptive unit, and other Cerro Negro eruptive units (Roggensack, unpublished data), do not encompass a large compositional range. However, in some cases, such as crystals #41 and #59 (Table 1), large compositional variation is observed. Crystal #41 is somewhat unusual in that it hosts numerous melt inclusions. One other exceptional crystal (#39) hosts two melt inclusions which are of apparently different genetic origin. Melt inclusion 39a has high TiO_2 while melt inclusion 39b has low TiO_2.

Table 2
Trace element abundances (ppm)

Sample	Li	B	Sr	Y	Zr	Ba	Ce
Melt inclusion analyses							
10	3.8	14	408	13	22	231	6.5
19	3.5	6	411	11	33	132	7.4
25	3.8	12	409	14	26	196	6.5
29	4.1	14	408	13	37	261	7.3
32[a]	3.8	11	398	13	22	178	5.3
33	4.2	16	366	12	24	193	4.6
35	3.6	6	405	13	40	193	9.5
36a	3.8	12	349	12	20	178	4.1
39a[b]	4.1	17	384	13	26	221	6.8
39b	3.8	17	365	13	24	206	7.2
41a[b]	5.9	18	415	16	30	273	7.2
41b	5.3	15	392	17	37	398	8.8
41c	5.1	15	386	19	38	340	9.5
45	3.6	12	384	13	25	197	6.3
51	3.1	19	411	11	22	208	4.9
59a	4.3	16	373	13	30	216	9.0
59b	3.9	15	347	10	18	191	5.1
65	3.5	10	371	12	20	204	4.9
66	3.9	14	426	13	22	207	7.2
70	3.7	12	396	13	23	201	5.5
71	3.3	17	471	16	28	260	7.7
72	3.8	15	389	14	22	208	5.5
73	2.8	4	510	10	6	53	1.5
74	3.9	17	423	17	21	212	5.8
75	3.3	15	412	11	25	203	6.0
104	7.1	17	394	23	48	484	10.6
Re-entrant analysis							
104RE	9.2	23	346	23	46	484	10.8
Bulk ash analyses							
CN	n.d.	n.d.	375	14	31	271	17
CN[c]	n.d.	n.d.	415	15	31	287	26

Melt inclusion and re-entrant analyses determined by ion probe. Bulk ash analyzed by XRF. n.d., not determined.
[a]Superscript identifies melt inclusions which contain daughter crystals of plagioclase.
[b]Superscript identifies melt inclusions which contain daughter crystals of magnetite.
[c]Large phenocrysts removed by handpicking.

A striking feature of the data is the apparent correlation between melt inclusion composition and host crystal size (Fig. 3). Excluding exceptionally large crystals (>25 mg), decreasing host crystal size correlates with increasing K_2O content of melt inclusions. This relationship seems to break down at very small crystal sizes (<2.7 mg) where a large melt inclusion compositional range is observed. Overall this trend mirrors

Table 3
Melt inclusion volatiles determined by FTIR Spectroscopy

Melt inclusions	Wafer thickness (μm)	OH (4500 cm^{-1}) (wt%)	H_2O mol (5200 cm^{-1}) (wt%)	H_2O mol (1630 cm^{-1}) (wt%)	H_2O_{total} [a] (wt%)	H_2O_{total} (3500 cm^{-1}) (wt%)	CO_2 (ppm)	Saturation pressure (kbar)
10	58	2.2	2.3	2.4	4.5	n.d.	479	3.2
19	80	2.5	2.6	2.9	5.1	n.d.	1113	5.1
29	180	2.4	2.8	n.d.	5.2	n.d.	437	3.9
32	180	2.3	2.4	n.d.	4.7	n.d.	806	4.1
33	84	2.2	2.9	3.0	5.1	n.d.	1053	5.0
35	80	2.5	3.4	3.5	6.0	n.d.	1024	5.8
36a	70	2.3	3.0	3.2	5.4	n.d.	975	5.2
39a	104	2.1	2.7	2.7	4.8	n.d.	683	3.9
39b	104	2.3	3.0	3.1	5.3	n.d.	691	4.5
41a	70	1.3	1.3	1.3	2.6	n.d.	127	1.0
41b	70	1.9	1.3	1.3	3.2	3.1	146	1.5
45	127	2.5	2.5	2.6	5.0	n.d.	551	3.9
59a	78	2.6	3.1	3.1	5.7	n.d.	570	4.9
59b	78	2.4	2.8	3.0	5.2	n.d.	596	4.2
66	88	2.8	3.2	3.5	6.0	n.d.	550	5.1
70	68	2.7	3.5	3.7	6.2	n.d.	1083	6.4
71	62	1.8	1.4	1.5	3.3	3.4	1101	3.5
72	200	2.5	3.5	n.d.	6.0	n.d.	768	5.4
73	80	2.0	2.1	2.4	4.2	n.d.	b.d.l.	1.9
75	184	2.3	2.9	n.d.	5.2	n.d.	705	4.4
84	68	1.6	1.3	1.3	2.9	3.0	126	1.2
95	34	n.d.	n.d.	n.d.	n.d.	4.2	b.d.l.	1.9
105	62	2.3	2.5	2.8	4.8	n.d.	562	3.8
112	136	2.3	2.2	n.d.	4.5	n.d.	b.d.l.	2.2

n.d., not determined. b.d.l., below detection limit.
[a] Sum of 4500 cm^{-1} and 5200 cm^{-1} data.

the simple model system described in Section 1. In contrast, the exceptionally large crystals (∼50 mg) show moderate variation (0.22–0.34 wt% K_2O) but are otherwise compositionally similar to other melt inclusions. The one exception is crystal #73 which has exceptionally low K_2O.

5. Melt inclusion volatiles

The melt inclusions contain high abundances of H_2O and CO_2 as determined by FTIR spectroscopy (Table 3). Most of the melt inclusions form a vertical array on a plot of H_2O against CO_2 (Fig. 5). The group of melt inclusions hosted by large crystal outliers (>25 mg) generally show high water contents (∼6 wt% H_2O) relative to the main group of crystals (<25 mg; ∼5 wt% H_2O). Volatile element saturation pressures, based on H_2O and CO_2 solubility [18,19], span

a wide range and correlate with crystal size (Fig. 6). With few exceptions, melt inclusions in large crystals, as well as the large crystal outliers (>25 mg), show high saturation pressures. With decreasing host crystal size, and increasing K_2O contents, the saturation pressures progressively decrease. The smallest crystals (<2.7 mg) are underrepresented because their size makes them difficult to prepare and analyze by FTIR spectroscopy. Available data suggest that these small crystals have the lowest saturation pressures.

In addition to H_2O and CO_2, the volatile elements S, Cl, and B were also measured in the melt inclusions (Tables 1 and 2). There is considerable S and Cl variation in low-K_2O melt inclusions. Other melt inclusions seem to show S decrease and Cl increase with increasing degree of fractionation (e.g. increasing K_2O). Boron does not show any clear correlation with fractionation index or saturation pressure.

6. Discussion

6.1. Magma evolution by in situ crystallization

One possible source of melt inclusion compositional variability is post-entrapment crystallization. This process was evaluated by adding olivine (1% increments) to restore Fe/Mg equilibrium between melt inclusions and host crystals. Using a K_D^{Fe-Mg} of 0.32 the potential amount of post-entrapment crystallization varies between 0 and 12%. This amount is even lower if FeO abundance in the melt inclusion is adjusted for fO_2. This result suggests that any compositional modification of melt inclusions by post-entrapment crystallization has been negligible.

Cerro Negro melt inclusions show large variations in K_2O relative to other major elements. This feature resembles the 'over-enrichment' seen in many MORB suites [20,21]. With one exception (#73; see below) the range in K_2O abundance defined by melt inclusions (0.19–0.74 wt% K_2O) would correspond to roughly 75% fractional crystallization. Although this is a staggering amount of crystallization it may be reasonable given the melt inclusion evidence that the Cerro Negro magma was volatile-rich. The decompression of

a volatile-bearing magma causes degassing which is accompanied by rise in liquidus temperature and crystallization [22]. Also, the highest K_2O melt inclusions are compositionally similar to matrix glass (Table 1). The implication is that the magma was quenched before it could completely crystallize and that the melt inclusions record crystallization almost to the point at which the magma solidified.

Simple least-squares models can be used to further test a fractional crystallization hypothesis. The models presented in Table 4 demonstrate that removal of an assemblage of plagioclase–clinopyroxene–olivine–magnetite can account for the observed compositional variation. Note that in order to achieve a good fit, these models require the use of low-temperature (or sub-liquidus) minerals since removal of higher-temperature minerals would deplete CaO and MgO in the magma without sufficiently enriching K_2O. Further evidence for possible sub-liquidus crystallization is apparent in the relationship between melt inclusions and the composition of their host crystals (Table 1). Some melt inclusions which have contrasting compositions (e.g. #19 and 29) are hosted by magnesian olivine (Fo_{81}).

Incompatible trace element abundances show

Table 4
Results of least-squares modeling for Cerro Negro melt inclusions

Mineral fraction		Mineral composition		Mineral fraction		Mineral composition	
0.295		Plag. (An_{70})		0.292		Plag. (An_{67})	
0.135		Cpx ($En_{42}Wo_{44}Fs_{14}$)		0.126		Cpx ($En_{42}Wo_{44}Fs_{14}$)	
0.061		Ol (Fo_{72})		0.005		Ol (Fo_{72})	
0.034		Mt		0.022		Mt	
0.478		Sample 87		0.553		Sample 104	
Sample:	87	95	(Calculated)	104	107	(Calculated)	
wt%							
SiO_2	51.07	48.18	48.11	53.23	50.72	50.76	
TiO_2	0.97	0.76	0.88	1.08	0.89	0.89	
Al_2O_3	16.01	17.69	17.63	15.71	18.30	18.32	
FeO	13.50	12.23	12.22	12.10	10.03	10.03	
MnO	0.29	0.24	0.20	0.25	0.18	0.17	
MgO	5.11	6.76	6.78	4.32	4.51	4.50	
CaO	9.92	11.89	11.91	9.68	12.11	12.10	
Na_2O	2.53	1.97	2.23	2.80	2.73	2.63	
K_2O	0.44	0.20	0.23	0.67	0.44	0.42	
P_2O_5	0.17	0.07	0.08	0.16	0.10	0.09	
Sum of squares of residuals		0.085				0.011	

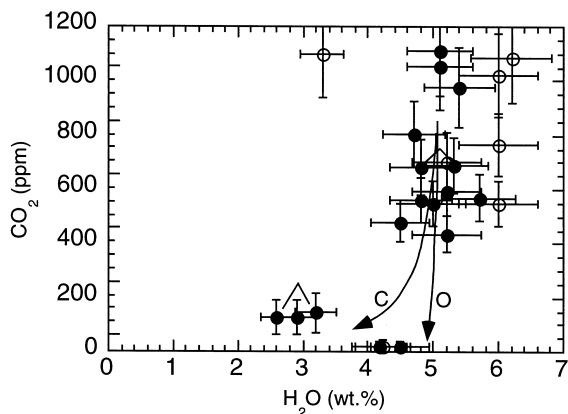Plag, plagioclase; Cpx, clinopyroxene; Ol, olivine; Mt, magnetite.

Fig. 5. H_2O and CO_2 variation in olivine melt inclusions. Unfilled circles identify melt inclusions hosted by large crystals (>25 mg). Tie-lines identify crystals hosting multiple melt inclusions. Closed-system (C; assumes initial condition of 1 wt% exsolved gas) and open-system (O) degassing trends are also shown.

behavior similar to that of K_2O. For instance, the elements Y and Zr correlate with K_2O. These relationships suggest that fractional crystallization is capable of explaining much of the compositional variation. Several melt inclusions have unique compositions that require a separate origin. The presence of high-TiO_2 and low-subduction-component melt inclusions (#39a and 73, respectively) in Cerro Negro's magma system will be addressed in a separate study (Roggensack, in preparation).

Evidence for crystallization of sub-liquidus phases and enrichment in incompatible elements despite modest major element variation are both key signatures of in situ crystallization [23]. The large variation in volatile saturation pressures and the apparent degassing trend (Fig. 5) suggest that the magma was ascending through the crust in a dike rather than ponding in a magma chamber. An ascending magma would encounter frequent thermal contrasts with wallrock resulting in crystallization being concentrated in boundary layers or 'solidification zones' along the walls of the dike. Evolved magma in these solidification zones could crystallize significant amounts of low-temperature mineral phases. In turn, the compositional variability of melt inclusions at particular depths (saturation pressures) most likely repre-

sents the interaction between magma within the interior of the dike and evolved magma returning from the solidification zones along the wall of the dike. Mixing between these magmas, and possibly relatively unfractionated magma rising from deeper levels, might generate significant short-term compositional fluctuations. More rigorous modeling of in situ crystallization [24] is beyond the scope of this study.

6.2. Open-system degassing and crystallization

If large crystal outliers are excluded, the H_2O abundance in Cerro Negro melt inclusions remains essentially constant as CO_2 decreases (Fig. 5). This type of CO_2-H_2O trend is a hallmark of open-system degassing [25] and suggests that the Cerro Negro magma was volatile-saturated (H_2O and CO_2). Melt inclusions hosted by large crystal outliers also seem to form an open-system degassing trend shifted toward high water abundance. The high volatile saturation pressures of melt inclusions hosted by large crystal outliers preclude any simple relationship to other melt inclusions. Compositional variation (K_2O 0.22–0.34 wt%; excluding #73) and the high water abundance of melt inclusions hosted by large crystal outliers could be due to enrichment by crystal fractionation ($\sim 35\%$) and magma re-charge and will be addressed in a separate study.

The inference that the magma was ascending through the crust as it evolved has implications for general igneous processes and the magma plumbing of Cerro Negro. It is common to assume that volcanoes that have numerous eruptions (i.e. polygenetic) are fed by magma chambers. This generally implies fixed pressures, temperatures buffered by thermal mass and periodic refilling. However, this study, along with previous work [8], indicates that Cerro Negro eruptions are fed by ephemeral dikes. Although all of the studied Cerro Negro eruptions may have ultimately been fed by deep magma chambers, >14 km for the present case (based on volatile saturation pressures; Fig. 6), it is significant that magma evolution and most likely eruptive triggering occurs within shallow dikes, not in a large volume magma chamber (conventional sense).
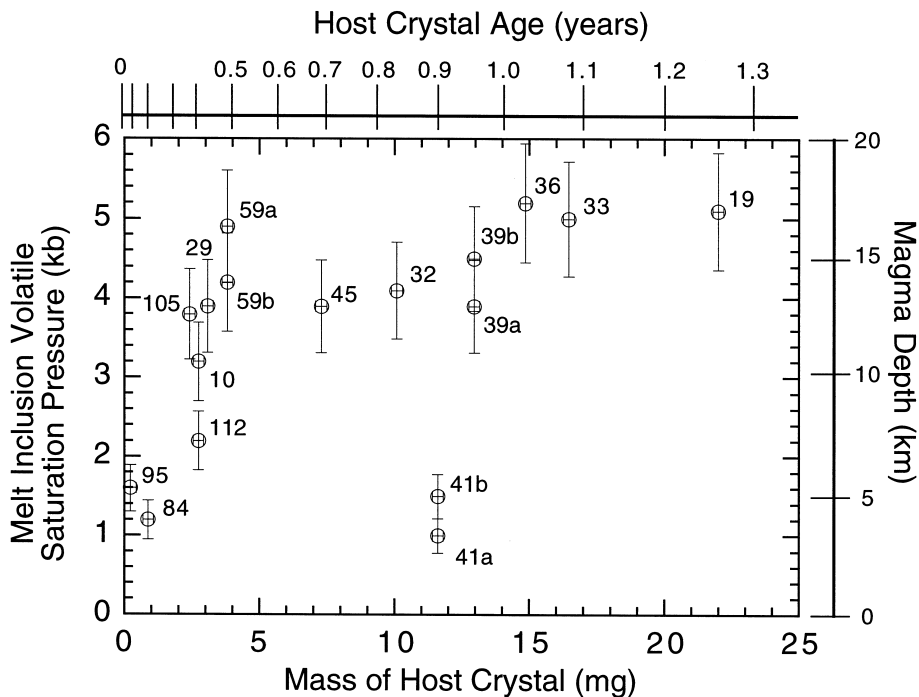
Fig. 6. Host crystal mass versus melt inclusion volatile saturation pressure as determined by H_2O and CO_2 solubility. Large crystal outliers (>25 mg) not shown. Crystal age was calculated assuming a constant crystal growth rate (see text and Appendix A). Depth is calculated from melt inclusion saturation pressures assuming 1 kbar equals ~ 3.3 km.

6.3. Significance of melt inclusions in small crystals

As discussed earlier, compositional variability is expected to be greatest in melt inclusions forming during later stages of crystallization because the magma composition changes more rapidly as the amount of remaining liquid declines. This scatter would be expected in the range of moderate to high K_2O (on or above the curve in Fig. 2). However, the combination of small crystals hosting low K_2O melt inclusions is in direct opposition to the general trend of increasing K_2O with decreasing crystal size (Fig. 3). It seems unlikely that all of the small crystals hosting low-K_2O melt inclusions are random xenocrysts. The large compositional zoning in small crystals might be explained by magma zoning but the K_2O content of matrix glass matches that found in highly evolved melt inclusions. This relationship severely limits the amount of low-K_2O magma present in the system prior to eruption. Instead, the small crystals (i.e. young in age) hosting low-K_2O melt

inclusions were probably introduced by a separate magma very late in the crystallization history. Continuous or sub-continuous replenishment of magma systems beneath volcanoes is to be expected. It may be that without such additional input a volatile-rich dike approaches critical crystallinity [26] and becomes incapable of erupting. The more general implication is that there is evidence for at least three different magmas within a single eruptive unit. In addition to the predominant magma, the small crystals with low-K_2O melt inclusions represent a second magma introduced late in the history of the dike and a third magma is represented by large crystal outliers. While previous studies have identified the interaction of multiple magmas [27], here it is documented on the scale of individual crystals.

6.4. CSD analysis

The theory of CSD analysis and geologic appli-

cations have been presented by a number of investigators [28–31]. CSD analysis is a means for monitoring the crystal population density during crystallization. Population density (n) can be defined in terms of the total number of crystals (N) and crystal size (i.e. length; L):

$$N(L) = \int n(L)\mathrm{d}L \text{ (evaluated from 0 to } L)$$

which becomes:

$$\mathrm{d}N(L)/\mathrm{d}L = n(L)$$

Extracting information on crystal growth rates and crystal nucleation rates from the population density requires the use of a conservation equation. Marsh [31] discusses conservation equations for a number of different types of geologically reasonable igneous systems. A generally applicable result from these examples is:

$$\ln(n) = -(1/G\tau)L + \ln(n^\circ)$$

$$J = n^\circ G$$

where G is crystal growth rate, τ represents the residence time of crystals in the system and J is nucleation rate. It should be noted that the population density and nucleation rate are referred to as *effective* values because the system may not truly be at steady state.

6.5. How representative is the sample population?

It is important to consider the influence that sampling errors might have on CSD analyses and the crystallization model. Mangan [32] has shown that traditional CSD analyses are quite robust for small sample populations, and demonstrated that a sample number of as few as 25 crystals can give consistent results. In addition to sample size, there is also the question of whether the magma sample is truly representative of the original magma. Magmas may be modified by crystal sorting and crystal settling. The melt inclusion–crystal size relationship (Fig. 3) and the large crystal size range suggest that crystal settling may only affect crystals larger than were observed.

One advantage of studying tephra deposits as opposed to lavas is that weighing individual crystals renders size reconstructions from 2-D thin sections [33] unnecessary. Also, the rapid quenching prevents subaerial crystallization that might otherwise continue in lava flows. The disadvantage of studying tephra deposits is that crystal sorting in the eruption column introduces another potential source of error [32]. To a large extent these errors can be eliminated by working on poorly sorted proximal deposits. Given that the present sample contains crystals and lapilli-size scoria up to $\sim$6 mm, it seems unlikely that sorting processes have modified the observed CSD.

6.6. Time of crystallization for Cerro Negro magma

A CSD plot for Cerro Negro crystals is shown in Fig. 7. The linear distribution revealed on this plot is typical of igneous CSDs [30]. Using the slope ($-1/G\tau$; Fig. 7) from the CSD plot and assuming a crystal growth rate G it is possible to estimate τ, the residence time for crystals in the magma. In the present case, the magma was moving through the crust as it crystallized so τ, the residence time, actually represents the time interval during which the magma rose through the crust. Olivine growth rates have been measured between 10^{-8} and 6×10^{-5} cm s^{-1} [3]. Using the slowest value of 10^{-8} cm s^{-1} for the Cerro Negro data yields an age of 0.5 years. This value can be adjusted to compensate for the difference between a spherical geometry and natural crystal shape by comparing calculated spherical diameters (assuming constant density of 3.45) with measured crystal lengths (Appendix A). A linear regression of these data ($R = 0.92$) indicates that crystal length is roughly $1.56\times$ spherical diameter. This would adjust the age calculated by CSD upwards to $\sim$0.8 years.

6.7. CSD kinks and the significance of large crystals

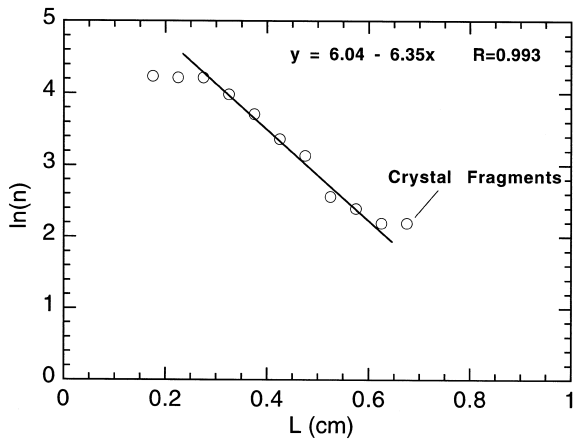Growth dispersion and crystal aggregation are

Fig. 7. CSD plot for Cerro Negro magma. The first two and last two points were not included in the regression. The kink at large L should be considered schematic given the error in size of large crystal fragments. Bin size was 0.05 cm. Crystal mass was first converted to spherical volume assuming a constant mineral density of 3.45 g cm^{-3}. Calculated diameters were converted to crystal lengths based upon a linear regression of crystal mass and measured crystal length (see Appendix A).

two processes which can greatly complicate the analysis of CSDs. Growth dispersion occurs when identical crystals under the same growth conditions grow at different rates [34]. Crystal aggregation, or synneusis [17], can also create discrepancies in crystal size distributions. The correlation between melt inclusion composition and host crystal size suggests that these processes did not significantly affect the Cerro Negro magma. Crystal aggregation in particular, should produce crystals with high K_2O that would plot above the main crystal weight–K_2O trend (Fig. 1). The only crystal that contains melt inclusions which plot significantly above the trend (#41) also contains melt inclusions that plot on the main trend. This crystal is either a xenocryst or may have repeatedly trapped magma over a large fractionation interval.

It can be seen from the CSD plot (Fig. 7) that the large crystal outliers create a kink in the otherwise log-linear CSD plot. The kink, which is problematic because of the poor size constraints of the large crystals, has important implications for the origins of the large crystals. In general,

CSD kinks of this type are interpreted as reflecting either a sudden change in nucleation rate or growth processes [31]. The CSD results seem to confirm the earlier textural and geochemical arguments that the large crystal outliers are not closely related to the predominant group of crystals (< 25 mg). Most likely the large outliers were picked up by the magma as it rose through the deep to middle crust.

6.8. Relationship between crystal and melt inclusion ages

As compared to the time required for crystallization indicated by conventional CSD analysis, the actual decompression history of the magma can be reconstructed by linking crystal size and melt inclusion information. The age of a crystal can be calculated by converting crystal mass to crystal length just as was done for the CSD analysis (see Appendix A). If a constant growth rate is assumed the age of the crystal can be directly determined. It should be noted that the primary assumptions involved in this calculation are the same as those commonly made for traditional CSD analysis: first, that the crystal size population represents magmatic conditions and second, that the crystal growth rate was constant.

In actuality, the concern is not the age of each crystal but the relative timing of melt inclusion entrapment. Relating melt inclusion age to crystal growth requires the assumption that the timing of melt inclusion formation is non-random. The relationships shown in Figs. 3 and 6 resemble the hypothetical model (Fig. 2) describing crystal size and melt inclusion composition. Large crystals host melt inclusions which are primitive (low K_2O) and have high volatile saturation pressures whereas the converse is true for small crystals. The implication is that melt inclusions generally form early in the crystal's history shortly after crystal nucleation. There are two apparent exceptions to the general relationship between crystal size and melt inclusion composition. One exception seems to be the rare case in which single crystals host multiple melt inclusions of contrasting composition. The other exception seems to be the small crystals which host low-K_2O melt inclu-

sions. It could be argued that both these exceptions are evidence of zoning within the magma and certainly some zoning is required of the in situ crystallization model. Since matrix glass composition is similar to evolved melt inclusions the compositional zoning in the dike is probably minor. The crystals with multiple and contrasting melt inclusions must have either trapped magma at different times or they record the interaction of several magmas. The small crystals with low-K_2O melt inclusions most likely represent a separate magma, although some means of poisoning crystal growth may also be possible.

6.9. Magma decompression history

Comparisons of eruption styles of silicic magmas and their volatile contents indicate that decompression history has an important influence on eruptive behavior [35]. The same is also true of mafic magmas [8]. The crystal ages shown on Fig. 6 are based solely on crystal size assuming a constant crystal growth rate of 10^{-8} cm s^{-1}, as was done for CSD analysis. If melt inclusion age is related simply to crystal age, as previously discussed, then Fig. 6 reveals the decompression history of Cerro Negro's magma. The magma ascended through the lower to middle crust ($\sim$12.5 to $\sim$16.8 km depth) over a roughly 0.9-year period (Fig. 6; Table 5) with an initial rate of magma ascent of $\sim$4.8 km yr^{-1}. The rate of magma ascent in the middle to upper crust was roughly an order of magnitude greater.

7. Summary

This study demonstrates how textural information can be linked with melt inclusion data to study igneous and volcanic processes. This approach can be used to 'image' magmas during their evolution and ascent through the Earth's crust. Melt inclusion data not only demonstrate that the Cerro Negro magma was volatile-rich but also record a significant decompression history. Traditional CSD analysis constrains the elapsed time of decompression whereas individual crystal model ages define an apparent *P–X–t* path.

The Cerro Negro magma was not fed by a large magma chamber in a 'conventional' sense. Instead, the magma traversed the crust in a dike and evolved by in situ crystallization. The absence of a magma chamber also has implications for how magmas erupt. This study and previous work [8] at Cerro Negro suggest that eruptive triggering occurs at variable depth within dikes, without any direct influence from a magma chamber. Other examples of volcanoes without upper crustal magma chambers have been recognized in Japan [36] and the Aleutians [37]. Models of eruptive triggering which involve magma chambers [38] will need revision to account for volcanoes fed by mobile, decompressing magmas.

It is certainly difficult to identify independent but compositionally similar components of mafic magmas, yet this information has important bearing on magma evolution, eruptive processes and volatile abundances. Although not a primary focus of this study, the results demonstrate how

Table 5
Estimates of magma ascent rate based on crystal growth rates (see text)

Crystal growth rate (cm s^{-1})	Transport age (years)	Initial ascent rate (cm s^{-1})	Average ascent rate (cm s^{-1})
10^{-6}	0.013	1.5×10^{0}	4.2×10^{0}
10^{-7}	0.13	1.5×10^{-1}	4.2×10^{-1}
10^{-8}	1.3	1.5×10^{-2}	4.2×10^{-2}
10^{-9}	12.6	1.5×10^{-3}	4.2×10^{-3}
10^{-10}	126	1.5×10^{-4}	4.2×10^{-4}

Other estimates of magma ascent rates: 10^{-1}–10^{-5} cm s^{-1}: Marsh [39]; 0.6–0.8 cm s^{-1}: Helz [40]; 1 cm s^{-1}: Sparks et al. [41]; 1–3000 cm s^{-1}: Spera [42].

textural evidence and melt inclusions may be used to aid this discrimination process. It has been found that a single eruptive deposit contains contributions from at least three distinct magmas.

8. Conclusions

This study demonstrates how crystal size temporally constrains melt inclusion compositions. At Cerro Negro the melt inclusions record the decompression and crystallization of a volatile-rich magma. Incorporation of crystal size information constrains this process and yields an apparent P–X–t path for the Cerro Negro magma. The ability to constrain melt inclusion relationships using crystal size may be of general use in other deposits. In addition to decompression history, this study has shown that crystal size relationships help to identify otherwise cryptic magma mixing events. Future studies might use crystal size to identify young melt inclusions in order to study late-stage magma processes.

#	Crystal mass (mg)	Crystal length (cm)	#	Crystal mass (mg)	Crystal length (cm)	#	Crystal mass (mg)	Crystal length (cm)
1	5.16	0.194	38	19.16	0.30	80	1.39	n.d.
2	1.08	0.128	39	12.96	0.28	81*	1.68	n.d.
3	18.49	n.d.	40	14.83	0.256	82	0.16 (5)	n.d.
4	12.99	n.d.	41*	11.60	n.d.	83	1.32	n.d.
5	7.07	0.20	42	4.41	0.182	84	0.88 (50)	n.d.
6	2.92	0.15	43	19.31	0.32	85	0.88	n.d.
7	5.66	0.18	44	5.58	0.24	86	0.13	n.d.
8	12.44	0.28	45	7.28	n.d.	87	0.48	n.d.
9	8.74	0.25	46	6.58	0.22	88	1.39 (20)	n.d.
10	2.74	n.d.	47	2.75	0.152	89	0.20 (20)	n.d.
11	7.03	0.256	48	3.29	n.d.	90	0.54 (5)	n.d.
12	16.45	0.27	49	6.89	0.234	91	2.40	n.d.
13	7.79	n.d.	50	15.20	0.272	92	0.71 (20)	n.d.
14	3.63	0.15	51	6.12	n.d.	93*	0.69	n.d.
15	30.24	0.448	52	9.30	n.d.	94	1.92 (5)	n.d.
16	6.99	0.232	53	16.10	0.35	95	0.23	n.d.
17	2.70	0.18	54	4.52	0.21	96*	0.17 (30)	n.d.
18	5.25	0.20	55	6.93	0.214	97	0.56 (25)	n.d.
19*	21.99	0.364	56	4.06	n.d.	98	1.43 (<5)	n.d.
20	2.87	0.132	57	3.16	0.16	99	1.15	n.d.
21	6.05	0.176	58	3.81	n.d.	100	1.30 (10)	n.d.
22	19.99	0.26	59	3.80	n.d.	101	1.29 (20)	n.d.
23	12.20	0.264	60	6.88	0.256	102	0.05 (10)	n.d.
24	3.37	0.194	61	3.52	0.188	103	0.77 (10)	n.d.
25	15.67	0.29				104	1.68 (25)	n.d.
26	3.25	0.156	65	~50.00	n.d.	105	2.41 (25)	n.d.
27	5.50	n.d.	66	~50.00	n.d.	106*	1.91 (<5)	n.d.
28	4.04	0.186	67	~50.00	n.d.	107	3.61 (10)	n.d.
29	3.07	0.18	68	~50.00	n.d.	108	1.56	n.d.
30	8.32	0.25	69	~50.00	n.d.	109	1.25	n.d.
31	5.31	0.19	70	~50.00	n.d.	110	1.83	n.d.
32	10.08	n.d.	71	~50.00	n.d.	111	2.11 (<5)	n.d.
33	16.46	0.27	72	~50.00	n.d.	112*	2.73	n.d.
34	3.35	0.172	73	~50.00	n.d.	113	1.19 (25)	n.d.
35	50.85	n.d.	74	~50.00	n.d.	114	2.35	n.d.
36	14.85	0.34	75	~50.00	n.d.			
37	28.63	n.d.	76	~50.00	n.d.			

*Crystal aggregates. n.d., not determined.

Acknowledgements

Appendix A. Olivine crystal mass and length

Mass values for broken crystals have been restored based on visual estimates of the euhedral fragments. Where applicable the amount of the correction (%) is listed in parentheses. Corrections of 5% or less were ignored. The series of crystals 65–76 represent exceptionally large fragments with little or no visible crystal form whose mass estimates are approximate. Crystal lengths were measured using an optical microscope. A linear regression of measured crystal length (Y) against calculated spherical diameter (X), assuming constant density of 3.45, yields: $Y = -0.021298 + 1.5597X$, $R = 0.92$.

References

[1] M. Hort, T. Spohn, Crystallization calculations for a binary magma cooling at constant rates of heat removal: implications for the crystallization of magma bodies, Earth Planet. Sci. Lett. 107 (1991) 463–474.

[2] W.D. Means, Y. Park, New experimental approach to understanding igneous texture, Geology 23 (1994) 323–326.

[3] A. Jambon, P. Lussiez, R. Clocchiatti, J. Weisz, J. Hernandez, Olivine growth rates in a tholeiitic basalt: An experimental study of melt inclusions in plagioclase, Chem. Geol. 96 (1992) 277–287.

[4] C.H. Donaldson, An experimental investigation of olivine morphology, Contrib. Mineral. Petrol. 57 (1976) 187–213.

[5] R.J. Kirkpatrick, Nucleation and growth of plagioclase, Makaopuhi and Alae lava lakes, Kilauea Volcano, Hawaii, Geol. Soc. Am. Bull. 88 (1977) 78–84.

[6] A.R. Philpotts, J. Shi, C. Brustman, Role of plagioclase crystal chains in the differentiation of partly crystallized basaltic magma, Nature 395 (1998) 343–346.

[7] J.A. Walker, M.J. Carr, Compositional variations caused by phenocryst sorting at Cerro Negro volcano, Nicaragua, Geol. Soc. Am. Bull. 97 (1986) 1156–1162.

[8] K. Roggensack, R.L. Hervig, S.B. McKnight, S.N. Williams, Explosive basaltic volcanism from Cerro Negro volcano: Influence of volatiles on eruptive style, Science 277 (1997) 1639–1642.

[9] S.B. McKnight, Geology and Petrology of Cerro Negro Volcano, Nicaragua, M.S., Arizona State University, Tempe, AZ, 1995.

[10] P.D. Ihinger, R.L. Hervig, P.F. McMillan, Analytical methods for volatiles in glasses, in: M.R. Carroll, J.R. Holloway (Eds.), Volatiles in Magmas, Am. Mineral. Rev. Mineral. 30 (1994) 67–121.

[11] C.M. Skirius, J.W. Peterson, A.T. Anderson, Homogenizing rhyolitic glass inclusions from the Bishop Tuff, Am. Mineral. 75 (1990) 1381–1393.

[12] J.E. Dixon, E. Stolper, J.R. Delaney, Infrared spectroscopic measurements of CO_2 and H_2O glasses in the Juan de Fuca Ridge basaltic glasses, Earth Planet. Sci. Lett. 90 (1998) 87–104.

[13] J.E. Dixon, E.M. Stolper, J.R. Holloway, An experimental study of water and carbon dioxide solubilities in mid-ocean ridge basaltic liquids. Part I: Calibration and solubility results, J. Petrol. 36 (1995) 1607–1631.

[14] G.J. Fine, E. Stolper, Carbon dioxide in basaltic glasses: concentrations and speciation, Earth Planet. Sci. Lett. 76 (1986) 263–278.

[15] E. Zinner, G. Crozaz, A method for the quantitative measurement of rare earth elements in the ion microprobe, Int. J. Mass Spectrom. Ion Process. 69 (1986) 17–38.

[16] B.E. Hill, C.B. Connor, M.S. Jarzemba, P.C. LaFemina, M. Navarro, W. Strauch, 1995 eruptions of Cerro Negro volcano, Nicaragua, and risk assessment for future eruptions, Geol. Soc. Am. Bull. 110 (1998) 1231–1241.

[17] K.R. Schwindinger, A.T. Anderson, Synneusis of Kilauea Iki olivines, Contrib. Mineral. Petrol. 103 (1989) 187–198.

[18] C.W. Burnham, Development of the Burnham model for prediction of H_2O solubility in magmas, in: M.R. Carroll, J.R. Holloway (Eds.), Volatiles in Magmas, Am. Mineral. Rev. Mineral. 30 (1994) 123–129.

[19] J.R. Holloway, J.G. Blank, Application of experimental results to C-O-H species in natural melts, in: M.R. Carroll, J.R. Holloway (Eds.), Volatiles in Magmas, Am. Mineral. Rev. Mineral. 30 (1994) 187–230.

[20] F.A. Frey, N. Walker, D. Stakes, S.R. Hart, R. Nielsen, Geochemical characteristics of basaltic glasses from the AMAR and FAMOUS axial valleys, Mid-Atlantic Ridge (36°–37° N): Petrogenetic implications, Earth Planet. Sci. Lett. 115 (1993) 117–136.

[21] R. Sours-Page, K.T.M. Johnson, R.L. Nielsen, J.L. Karsten, Local and regional variation of MORB parent mag-

mas: evidence from melt inclusions from the Endeavor Segment of the Juan de Fuca Ridge, Contrib. Mineral. Petrol. 134 (1999) 342–363.

[22] C.W. Burnham, N.F. Davis, The role of H_2O in silicate melts: II. Thermodynamic and phase relations in the system $NaAlSi_3O_8$–H_2O to 10 kilobars, 700°C–1100°C, Am. J. Sci. 274 (1974) 902–940.

[23] C.H. Langmuir, Geochemical consequences of in situ crystallization, Nature 340 (1989) 199–205.

[24] R.L. Nielsen, S.E. DeLong, A numerical approach to boundary layer fractionation: Application to differentiation in natural magma systems, Contrib. Mineral. Petrol. 110 (1992) 355–369.

[25] J.E. Dixon, E.M. Stolper, An experimental study of water and carbon dioxide solubilities in mid-ocean ridge basaltic liquids. Part II: Applications to degassing, J. Petrol. 36 (1995) 1633–1646.

[26] B.D. Marsh, On the crystallinity, probablility of occurrence, and rheology of lava and magma, Contrib. Mineral. Petrol. 78 (1981) 85–98.

[27] M.K. Reagan, J.B. Gill, E. Malavassi, M.O. Garcia, Changes in magma composition at Arenal volcano, Costa Rica, 1968–1985: Real-time monitoring of open-system differentiation, Bull. Volcanol. 49 (1987) 415–434.

[28] A.D. Randolph, M.A. Larson, Theory of Particulate Processes, Academic Press, New York, 1988, 369 pp.

[29] K.V. Cashman, B.D. Marsh, Crystal size distribution (CSD) in rocks and the kinetics and dynamics of crystallization. II: Makaopuhi lava lake, Contrib. Mineral. Petrol. 99 (1988) 292–305.

[30] B.D. Marsh, Crystal size distribution (CSD) in rocks and the kinetics and dynamics of crystallization, Contrib. Mineral. Petrol. 99 (1988) 277–291.

[31] B.D. Marsh, On the interpretation of crystal size distributions in magmatic systems, J. Petrol. 39 (1998) 553–599.

[32] M.T. Mangan, Crystal size distribution systematics and the determination of magma storage times: The 1959 eruption of Kilauea volcano, Hawaii, J. Volcanol. Geotherm. Res. 44 (1990) 295–302.

[33] T.D. Peterson, A refined technique for measuring crystal size distributions in thin section, Contrib. Mineral. Petrol. 124 (1996) 395–405.

[34] J.W. Mullin, Crystallization, Butterworth-Heinemann, Boston, MA, 1993, 527 pp.

[35] C.R. Bacon, S. Newman, E. Stolper, Water, CO_2, Cl, and F in melt inclusions in phenocrysts from three Holocene explosive eruptions, Crater Lake, Oregon, Am. Mineral. 77 (1992) 1021–1030.

[36] T. Kuritani, Phenocryst crystallization during ascent of alkali basalt magma at Rishiri Volcano, northern Japan, J. Volcanol. Geotherm. Res. 88 (1999) 77–97.

[37] J.G. Brophy, C.S. Whittington, Y.-R. Park, Sector-zoned augite megacrysts in Aleutian high alumina basalts: implications for the conditions of basalt crystallization and the generation of calc-alkaline series magmas, Contrib. Mineral. Petrol. 135 (1999) 277–290.

[38] A.W. Woods, S.S.S. Cardoso, Triggering basaltic volcanic eruptions by bubble-melt separation, Nature 385 (1997) 518–520.

[39] B.D. Marsh, On the cooling of ascending andesitic magma, Phil. Trans. R. Soc. London A 288 (1978) 611–625.

[40] R.T. Helz, Diverse olivine types in lava of the 1959 eruption of Kilauea volcano and their bearing on eruption dynamics, in: Volcanism in Hawaii, U.S. Geological Survey Professional Paper 1350 (1987) 691–722.

[41] R.S.J. Sparks, H. Pinkerton, R. MacDonald, Transport of xenoliths in magmas, Earth Planet. Sci. Lett. 35 (1977) 234–238.

[42] F.J. Spera, Carbon dioxide in petrogenesis III: role of volatiles in the ascent of alkaline magma with special reference to xenolith bearing mafic lavas, Contrib. Mineral. Petrol. 88 (1984) 217–232.